ORIGINAL PAPER



How viscous is the beating heart? Insights from a computational study

Oğuz Ziya Tikenoğulları¹ · Francisco Sahli Costabal² · Jiang Yao³ · Alison Marsden⁴ · Ellen Kuhl¹

Received: 24 March 2022 / Accepted: 8 April 2022 / Published online: 13 May 2022 © The Author(s), under exclusive licence to Springer-Verlag GmbH Germany, part of Springer Nature 2022

Abstract

Understanding tissue rheology is critical to accurately model the human heart. While the elastic properties of cardiac tissue have been extensively studied, its viscous properties remain an issue of ongoing debate. Here we adopt a viscoelastic version of the classical Holzapfel Ogden model to study the viscous timescales of human cardiac tissue. We perform a series of simulations and explore stress—relaxation curves, pressure—volume loops, strain profiles, and ventricular wall strains for varying viscosity parameters. We show that the time window for model calibration strongly influences the parameter identification. Using a four-chamber human heart model, we observe that, during the physiologically relevant time scales of the cardiac cycle, viscous relaxation has a negligible effect on the overall behavior of the heart. While viscosity could have important consequences in pathological conditions with compromised contraction or relaxation properties, we conclude that, for simulations within the physiological range of a human heart beat, we can reasonably approximate the human heart as hyperelastic.

Keywords Cardiac mechanics · Human heart · Myocardium · Viscoelasticity · Finite element method

1 Motivation

Heart disease is the leading cause of death and disability in the world, accounting for approximately 40% of all human mortality generating an annual health care cost in excess of \$400 billion [1]. Its prevention and treatment have the utmost importance from a medical and economical point of view. Computational modeling is an emerging approach that helps clinicians with prevention and treatment of heart diseases [5,49]. Clinicians benefit from computational models when internal metrics of heart are impossible to measure or surgical planning is challenging without risking the patient's life. When the complex anatomy of the heart and its electromechanical function degenerate, for example in myocardial infarction [6] and heart failure [16], computational models offer a deeper insight that conventional methods cannot. The

- ⊠ Ellen Kuhl ekuhl@stanford.edu
- Department of Mechanical Engineering, Stanford University, Stanford, CA, USA
- Department of Mechanical and Metallurgical Engineering and Institute for Biological and Medical Engineering, Pontificia Universidad Catolica de Chile, Santiago, Chile
- Dassault Systèmes Simulia Corporation, Johnston, RI, USA
- Departments of Pediatrics and Bioengineering, Stanford University, Stanford, CA, USA

recent advancements in multiphysics modeling [18], fluid-structure modeling [32] and patient-specific modeling tools [10,49] are now making personalized heart simulations more affordable than ever.

Characterizing the passive mechanical response of the tissue is key to accurately model the human heart. The cardiac modeling community has broadly adopted a hyperelastic finite-strain continuum framework to represent the mechanical behavior myocardial tissue. Current models of cardiac mechanics account for compressibility [33] combined with a transversely isotropic [30] and orthotropic [19,29] behavior. However, including compressibility in conjunction with a volumetric-isochoric decomposition is not trivial and has been addressed in several recent studies [13,24,25]. Historically, ex-vivo mechanical testing of cardiac tissue samples has been used to calibrate the parameters of these models [14,46]. There is a recent focus on using inverse modeling to identify the in-vivo material properties of the living heart by comparing whole heart measurements to computational simulations [16]. These techniques can be combined with machine learning tools [2] to characterize whole ranges of material parameters along with their uncertainties [39].

One open question in the quest to understand the mechanics of the human heart is the importance of transient effects. Similar to most soft tissues in human body, in relaxation and creep tests, cardiac tissue displays a time-dependent mechan-

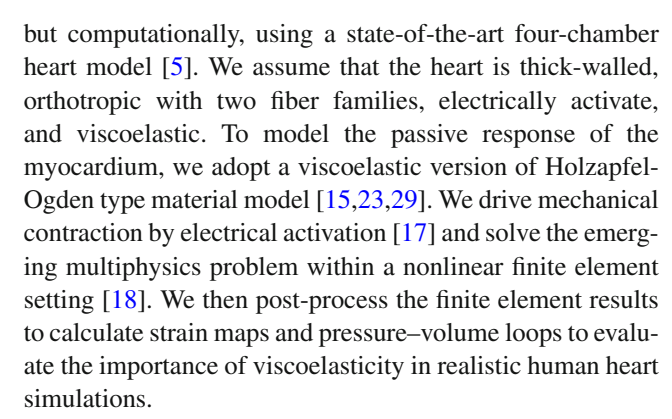


ical behavior. These transient effects become important at certain time scales and under specific loading conditions; therefore this phenomenon should be reflected in an accurate simulation of cardiac mechanics. On the structural level, the time-dependent response is represented through the inertia terms of a dynamic simulation [44]. On the constitutive level, transient response is related to viscoelastic effects, which can be attributed to macro- and micro-structural properties of the tissues, including poroelasticity [51], collagen fiber content [48] and titin-actin interaction [21]. Recent attempts focus on understanding the time-dependent viscoelastic response with experiments and replicating those with computational models. Several research groups have investigated the viscoelastic behavior of animal and human cardiac tissue samples in laboratory experiments [14,42,45,52].

Viscoelastic models for passive viscoelastic myocardium can be distinguished in two classes: The first class of models uses kinematic internal variables to track the viscous deformation history, for example to model the transversely isotropic [35] or orthotropic [7] response. In this approach, a dissipation potential characterizes the evolution of the internal variables. The second class of models uses stress-type internal variables, for example to model the isotropic [27], transversely isotropic [31] and orthotropic [23] response. In this approach, the stress consists of equilibrium nonequilibrium parts and the evolution of the non-equilibrium stress results from convolution integrals. Here, we adopt a viscoelastic constitutive model of the second class, which uses the convolution integral approach to evolve the stresslike viscous internal variables [23] and features a baseline hyperelastic formulation that accounts for fiber dispersion [15].

To model active muscle tissue contraction, we can use active strain or active stress methods. Active strain methods are motivated by microstructural mechanics and use the multiplicative decomposition of the deformation gradient into elastic and active parts [4]. This concept can be complemented by a generalized Hill model [26] that uses an additive decomposition of the stresses [20]. The generalized Hill model has proven successful in modeling cardiac dysfunction [6] and large strain electro-visco-elasticity [8]. Active stress methods, on the contrary, are a convenient phenomenological approach to reproduce active contractions. They simply superpose an active stress component over a passive stresses [34]. Here, we adopt the active stress method because its modular nature allows us to independently calibrate the active response from pressure-volume data and the passive response from separate experiments.

Here we build on the recent advancements in the experimental characterization and material modeling of human heart tissue to explore the role of viscoelasticity in cardiac simulations. The significance of this study lies in exploring the importance of viscosity, not experimentally in the lab,



This manuscript is organized as follows: In Sect. 2, we state the problem of cardiac electromechanics and outline our passive and active material modeling approach in a nonlinear continuum setting. In Sect. 3, we discuss the spatial and temporal discretizations of the problem and introduce our four-chamber finite element heart model. Section 4 presents the simulation results of the proposed computational model. Specifically, we determine and analyze different sets of parameters motivated by tissue characterization tests reported in the literature. We compare the different parameter sets by means of full heart simulations. We conclude by discussing the implications of our study and adding some final remarks in Sect. 5.

2 Continuum model

2.1 Kinematics

We consider the beating heart at time $t \subset \mathcal{R}$ as a continuum body in the three-dimensional space, $\mathcal{B} \subset \mathcal{R}^3$. We introduce the reference configuration as the body at initial time \mathcal{B}_0 . The mapping $\varphi(\mathcal{B}, t)$, maps a material point in the reference configuration $\mathbf{X} \in \mathcal{B}_0$ to its counterpart in the deformed configuration $\mathbf{x} \in \mathcal{B}$,

$$\varphi: \begin{cases} \mathcal{B}_0 \times \mathcal{T} \to \mathcal{B} \subset \mathcal{R}^3 \\ (\mathbf{X}, t) \mapsto \mathbf{x} = \varphi(\mathbf{X}). \end{cases}$$
 (1)

The deformation gradient **F** is the gradient of current position with respect to reference position,

$$\mathbf{F} = \nabla_{\mathbf{X}} \boldsymbol{\varphi}(\mathbf{X}, t) \text{ and } J = \det(\mathbf{F}),$$
 (2)

where J is the Jacobian of the deformation gradient, such that \mathbf{F} , $\operatorname{cof}(\mathbf{F})$ and J map material line elements, area elements, and volume elements into current configuration,

$$d\mathbf{x} = \mathbf{F} \cdot d\mathbf{X}$$
 $d\mathbf{a} = \operatorname{cof}(\mathbf{F}) \cdot d\mathbf{A}$ $dv = J \, dV$. (3)



The multiplicative decomposition of deformation gradient,

$$\mathbf{F} = \bar{\mathbf{F}} \cdot \mathbf{F}_{\text{vol}} \,, \tag{4}$$

introduces a spherical tensor that represents the volumetric part of deformation gradient and a unimodular tensor that represents the isochoric part,

$$\mathbf{F}_{\text{vol}} = \det(\mathbf{F})^{1/3}$$
 and $\bar{\mathbf{F}} = \mathbf{F} \cdot \mathbf{F}_{\text{vol}}^{-1} = \det(\mathbf{F})^{-1/3} \mathbf{F}$. (5)

The associated right Cauchy-Green deformation tensor ${\bf C}$ and its isochoric counterpart $\bar{{\bf C}}$ take the following form,

$$\mathbf{C} = \mathbf{F}^{\mathsf{t}} \cdot \mathbf{F} \quad \text{and} \quad \bar{\mathbf{C}} = J^{-2/3} \mathbf{C} \,.$$
 (6)

It proofs convenient to introduce six invariants related to these deformation tensors,

$$I_{1} = \mathbf{C} : \mathbf{I} \quad \bar{I}_{4f} = \bar{\mathbf{C}} : \mathbf{f}_{0} \otimes \mathbf{f}_{0} \quad I_{3} = \det(\mathbf{C}) = J^{2}$$

$$\bar{I}_{1} = \bar{\mathbf{C}} : \mathbf{I} \quad \bar{I}_{4s} = \bar{\mathbf{C}} : \mathbf{s}_{0} \otimes \mathbf{s}_{0} \quad \bar{I}_{8fs} = \operatorname{sym}(\bar{\mathbf{C}} : \mathbf{f}_{0} \otimes \mathbf{s}_{0}),$$
(7)

where \mathbf{I} is the second-order unit tensor and \mathbf{f}_0 and \mathbf{s}_0 are the fiber orientations in the reference configuration. These invariants complement the idea of the kinematic decomposition of deformation gradient; J, \bar{I}_1 , \bar{I}_{4f} , \bar{I}_{4s} and \bar{I}_{8fs} are measures of volumetric and isochoric deformations and of the isochoric stretch in the fiber and cross-fiber directions. The invariants \bar{I}_{4f} , \bar{I}_{4s} , and \bar{I}_{8fs} are calculated in Lagrangian fashion using the unrotated fiber orientations in the reference configuration, \mathbf{f}_0 and \mathbf{s}_0 . Importantly, the intermediate and deformed fiber orientations $\mathbf{f} = \bar{\mathbf{F}} \cdot \mathbf{f}_0/||\bar{\mathbf{F}} \cdot \mathbf{f}_0||$ and $\mathbf{s} = \bar{\mathbf{F}} \cdot \mathbf{s}_0/||\bar{\mathbf{F}} \cdot \mathbf{s}_0||$ are equivalent because the deformation between these two configurations is assumed to be purely volumetric. To incorporate fiber dispersion, we modify the definition of the structural tensors [15], and the dispersed fiber stretches are

$$\bar{I}_{4f}^* = \kappa_f \bar{I}_1 + [1 - 3\kappa_f] \bar{I}_{4f} \text{ and } \bar{I}_{4s}^* = \kappa_s \bar{I}_1 + [1 - 3\kappa_s] \bar{I}_{4s}.$$
(8)

Here κ_f , $\kappa_s \in [0, 1/3]$ are the dispersion parameters, where 0 represents perfectly aligned fibers whereas 1/3 recovers the isotropic response due to heavily dispersed fibers.

2.2 Balance equation

The balance of linear momentum defines the mechanical equilibrium in the geometrically nonlinear setting,

$$\rho_0 \ddot{\boldsymbol{\varphi}} = \text{Div}(\mathbf{F} \cdot \mathbf{S}) + \mathbf{F}^{\boldsymbol{\varphi}} \qquad \text{in } \mathcal{B}_0, \tag{9}$$

where **S** is the second Piola Kirchhoff stress tensor, \mathbf{F}^{φ} is the body force vector, and ρ_0 is the material density in reference

configuration. The balance equation is supplemented by the essential and natural boundary conditions, $\varphi = \overline{\varphi}$ on $\partial \mathscr{B}_0^{\varphi}$ and $\mathbf{S} \cdot \mathbf{N} = \overline{\mathbf{T}}$ on $\partial \mathscr{B}_0^T$, with the prescribed displacement $\overline{\varphi}$ and surface traction vector $\overline{\mathbf{T}}$.

2.3 Constitutive model

We model the electro-active behavior of cardiac tissue through passive and active stresses, $\mathbf{S} = \mathbf{S}_{pas} + \mathbf{S}_{act}$, and further decompose the passive stress into volumetric elastic, isochoric elastic, and viscous parts, $\mathbf{S}_{pas} = \mathbf{S}_{vol} + \mathbf{S}_{iso} + \mathbf{S}_{vsc}$, such that the overall second Piola Kirchhoff stress consists of four contributions,

$$\mathbf{S} = \mathbf{S}_{\text{vol}} + \mathbf{S}_{\text{iso}} + \mathbf{S}_{\text{vsc}} + \mathbf{S}_{\text{act}}. \tag{10}$$

We briefly describe all four stress terms in the following subsections.

2.3.1 Volumetric elastic stress

The volumetric elastic stress derives from the volumetric part of the free energy density function,

$$\psi_{\text{vol}} = \frac{1}{2} \kappa \left[\frac{1}{2} [J^2 - 1] - \ln(J) \right],$$
(11)

as a function of the Jacobian J and the initial bulk modulus κ . Consequently, the volumetric second Piola Kirchhoff stress,

$$\mathbf{S}_{\text{vol}} = 2 \frac{\partial \psi_{\text{vol}}}{\partial \mathbf{C}} = J \, S_J \, \mathbf{C}^{-1} \,, \tag{12}$$

becomes a function of the derivative of the volumetric free energy (11),

$$S_J = \frac{\partial \psi_{\text{vol}}}{\partial J} \,. \tag{13}$$

The volumetric elastic tangent moduli,

$$\mathbb{C}_{\text{vol}} = 2 \frac{\partial \mathbf{S}_{\text{vol}}}{\partial \mathbf{C}} = 2 \left[J^2 S_J' + J S_J \right] \mathbf{C}^{-1} \otimes \mathbf{C}^{-1} + J S_J \mathbb{I}_{\mathbf{C}^{-1}}$$
(14)

follow from the derivative of the elastic volumetric stress S_{vol} with respect to the Cauchy Green deformation tensor C, in terms of the second derivative,

$$S_J' = \frac{\partial^2 \psi_{\text{vol}}}{\partial J^2},\tag{15}$$

and the fourth order tensor $\mathbb{I}_{\mathbb{C}^{-1}} = \partial \mathbb{C}^{-1} / \partial \mathbb{C}$.



2.3.2 Isochoric elastic stress

The isochoric elastic stress follows from the isochoric part of the free energy density,

$$\psi_{iso} = \frac{a}{2b} [\exp(b(\bar{I}_1 - 3)) - 1]$$

$$+ \frac{a_f}{2b_f} [\exp(b_f(\bar{I}_{4f}^* - 1)^2) - 1]$$

$$+ \frac{a_s}{2b_s} [\exp(b_s(\bar{I}_{4s}^* - 1)^2) - 1]$$

$$+ \frac{a_{fs}}{2b_{fs}} [\exp(b_{fs}\bar{I}_{8fs}^2) - 1] ,$$
(16)

and is the projection of the intermediate stress \bar{S}_{iso} using the four-order projection tensor, $\mathbb{I}_{\bar{C}} = \partial \bar{C}/\partial C$,

$$\mathbf{S}_{\text{iso}} = 2 \frac{\partial \psi_{\text{iso}}}{\partial \mathbf{C}} = \bar{\mathbf{S}}_{\text{iso}} : \mathbb{I}_{\bar{\mathbf{C}}}.$$
 (17)

The stresses in the intermediate configuration take the following explicit representation,

$$\bar{\mathbf{S}}_{\text{iso}} = 2 \left[S_1 \mathbf{I} + S_{4f} \, \mathbf{f}_0 \otimes \mathbf{f}_0 + S_{4s} \, \mathbf{s}_0 \otimes \mathbf{s}_0 + S_{8fs} (\mathbf{f}_0 \otimes \mathbf{s}_0)^{\text{sym}} \right], \tag{18}$$

in terms of the four scalars,

$$S_{1} = \frac{\partial \psi_{\text{iso}}}{\partial \bar{I}_{1}} + \kappa_{\text{f}} \frac{\partial \psi_{\text{iso}}}{\partial \bar{I}_{4\text{f}}^{*}} + \kappa_{\text{s}} \frac{\partial \psi_{\text{iso}}}{\partial \bar{I}_{4\text{s}}^{*}} \qquad S_{8\text{fs}} = \frac{\partial \psi_{\text{iso}}}{\partial \bar{I}_{8\text{fs}}}$$

$$S_{4\text{f}} = \frac{\partial \psi_{\text{iso}}}{\partial \bar{I}_{4\text{f}}^{*}} [1 - 3\kappa_{\text{f}}] \qquad S_{4\text{s}} = \frac{\partial \psi_{\text{iso}}}{\partial \bar{I}_{4\text{s}}^{*}} [1 - 3\kappa_{\text{s}}]. \quad (19)$$

The isochoric elastic tangent moduli,

$$\bar{\mathbb{C}}_{iso} = 2 \frac{\partial \bar{\mathbf{S}}_{iso}}{\partial \bar{\mathbf{C}}} = 4 \left[S'_{1} \mathbf{I} \otimes \mathbf{I} + S'_{4f} \mathbf{f}_{0} \otimes \mathbf{f}_{0} \otimes \mathbf{f}_{0} \otimes \mathbf{f}_{0} \right. \\
+ S'_{4s} \mathbf{s}_{0} \otimes \mathbf{s}_{0} \otimes \mathbf{s}_{0} \otimes \mathbf{s}_{0} \\
+ S'_{8fs} (\mathbf{f}_{0} \otimes \mathbf{s}_{0})^{sym} \otimes (\mathbf{f}_{0} \otimes \mathbf{s}_{0})^{sym} \right]$$
(20)

follow from the derivative of the elastic isochoric stress $S_{\rm iso}$ with respect to the isochoric Cauchy Green deformation tensor \bar{C} , in terms of the second derivatives,

$$S'_{1} = \frac{\partial^{2} \psi_{\text{iso}}}{\partial \bar{I}_{1}^{2}} + \kappa_{\text{f}} \frac{\partial^{2} \psi_{\text{iso}}}{\partial \bar{I}_{4\text{f}}^{*2}} + \kappa_{\text{s}} \frac{\partial^{2} \psi_{\text{iso}}}{\partial \bar{I}_{4\text{s}}^{*2}} \qquad S'_{8\text{fs}} = \frac{\partial^{2} \psi_{\text{iso}}}{\partial \bar{I}_{8\text{fs}}^{2}}$$

$$S'_{4\text{f}} = \frac{\partial^{2} \psi_{\text{iso}}}{\partial \bar{I}_{4\text{f}}^{*2}} [1 - 3\kappa_{\text{f}}] \qquad S'_{4\text{s}} = \frac{\partial^{2} \psi_{\text{iso}}}{\partial \bar{I}_{4\text{s}}^{*2}} [1 - 3\kappa_{\text{s}}]. \tag{21}$$



Unlike the elastic response, the viscous response is history-dependent. The treatment of the history-dependent variable, the viscous stress S_{vsc} , requires a rate-type evolution equation and its integration across the time domain. Here we select a linear first-order differential equation to characterize the evolution of the viscous stress [23],

$$\dot{\bar{\mathbf{S}}}_{\text{vsc}} + \frac{1}{\tau} \bar{\mathbf{S}}_{\text{vsc}} = \beta \, \dot{\bar{\mathbf{S}}}_{1} \tag{22}$$

where τ is the relaxation time with unit of time, β is the dimensionless viscosity factor, and $\bar{\mathbf{S}}_1 = 2 S_1 \mathbf{I}$ is the elastic stress of equation (18). We substitute and re-write the viscous stress evolution $\dot{\mathbf{S}}_{\text{vsc}}$ from equation (22) in exact closed-form expression,

$$\bar{\mathbf{S}}_{\text{vsc}} = \int_{0}^{t} \exp\left(-\frac{t-s}{\tau}\right) \beta \,\dot{\bar{\mathbf{S}}}_{1} \,\mathrm{ds}\,,\tag{23}$$

and assume that the initial configuration is viscous-stress free, $\bar{\mathbf{S}}_{\text{vsc}}(t=0) = \mathbf{0}$. To discretize the viscous evolution in time, we consider time intervals $[0, t_n]$ and $[t_n, t]$ within the time domain of interest and define the time step $\Delta t = t - t_n$. Following the standard procedure [28], we identify a convolution integral form, approximate it using the mid-point rule, and perform standard numerical integration [23],

$$\bar{\mathbf{S}}_{\text{vsc}} = \exp\left(-\frac{\Delta t}{2\tau}\right) \left[\exp\left(-\frac{\Delta t}{2\tau}\right) \bar{\mathbf{S}}_{\text{vsc}}^{n} - \beta \left[\bar{\mathbf{S}}_{1}^{n} - \bar{\mathbf{S}}_{1}\right]\right]. \tag{24}$$

Here, $\bar{\mathbf{S}}_1^n$ and $\bar{\mathbf{S}}_{\text{vsc}}^n$ denote the elastic and viscous stresses at the previous time point t_n , while $\bar{\mathbf{S}}_1$ and $\bar{\mathbf{S}}_{\text{vsc}}$ denote the stresses at the current time point t. Note that we do not need to compute the convolution integral $\bar{\mathbf{S}}_{\text{vsc}}^n = \int_0^{t_n} \exp(-[t_n - s]/\tau) \beta \, \bar{\mathbf{S}}_1 \, ds$, because $\bar{\mathbf{S}}_1^n$ and $\bar{\mathbf{S}}_{\text{vsc}}^n$ become the history variables and are known at the previous time point t_n . The viscous contribution to the material tangent,

$$\bar{\mathbb{C}}_{\text{vis}} = \exp\left(-\frac{\Delta t}{2\tau}\right) \beta \bar{\mathbb{C}}_1 \quad \bar{\mathbb{C}}_1 = 2\frac{\partial \bar{\mathbf{S}}_1}{\partial \bar{\mathbf{C}}} = 4 \, S_1' \mathbf{I} \otimes \mathbf{I} \quad (25)$$

is fairly straightforward since it does not dependent on the loading history. For our the special case of our model, the tensor variables in equations (24) and (25) are co-axial and we can simplify them to the following format,

$$\bar{\mathbf{S}}_1 = S_1 \mathbf{I} \quad \bar{\mathbf{S}}_{\text{vsc}} = S_{\text{vsc}} \mathbf{I} \quad \bar{\mathbb{C}}_{\text{vis}} = 4S'_{\text{vsc}} \mathbf{I} \otimes \mathbf{I}.$$
 (26)

This reduces the number of internal variables from 12, i.e., six for $\bar{\mathbf{S}}$ and six for $\bar{\mathbf{S}}_{vsc}$, to just two for S_1 and S_{vsc} . The updates



of equations (24) and (25) then reduce to the following scalar expressions,

$$S_{\text{vsc}} = \exp\left(-\frac{\Delta t}{2\tau}\right) \left[\exp\left(-\frac{\Delta t}{2\tau}\right) Q^n - \beta \left[S_1^n - S_1\right]\right]$$

$$S_{\text{vsc}}' = \exp\left(-\frac{\Delta t}{2\tau}\right) \beta S_1'. \tag{27}$$

We denote that using multiple viscous terms, and with it multiple relaxation times τ and viscosity factors β , would improve the approximation of experimental data; however, here, we use a single viscous term to illustrate its physical interpretation in view of the human heart.

2.3.4 Active stress

We assume that active tissue contraction is generated by an active traction force $S_{\rm act}$ that acts along the muscle fiber direction \mathbf{f}_0 . The active part of the second Piola–Kirchhoff tensor $\mathbf{S}_{\rm act}$ then takes the following simple form,

$$\mathbf{S}_{\text{act}} = S_{\text{act}} \, \mathbf{f}_0 \otimes \mathbf{f}_0 \,. \tag{28}$$

For the active traction force S_{act} , we assume a time-varying elastance model [22,50],

$$S_{\text{act}} = S_{\text{max}} \frac{\text{Ca}_0^2}{\text{Ca}_0^2 + \text{ECa}_{50}^2} [1 - \cos(\omega)] \qquad S'_{\text{act}} = \frac{\partial S_{\text{act}}}{\partial \bar{I}_{4f}}.$$
(29)

where Ca_0 is the peak intercellular calcium concentration and ECa_{50} is

ECa₅₀ =
$$\frac{\text{Ca}_{0 \text{ max}}}{\exp[B(l-l_0)]-1}$$
 with $l = l_R \sqrt{\bar{l}_{4f}}$. (30)

 $S_{\rm max}$ is the maximum tension, ${\rm Ca_{0\,max}}$ is the maximum intercellular calcium concentration, l_R is the initial sarcomere length, and l_0 is the minimum sarcomere length. The angle ω in equation (28) is

$$\omega = \begin{cases} \pi \ t/t_0 & \text{when } 0 \le t \le t_0 \\ \pi \ [t - t_0 + t_r]/t_r & \text{when } t_0 \le t \le t_0 + t_r \\ 0 & \text{when } t \ge t_0 + t_r \end{cases}$$
(31)

with $t_r = m l + b$, where t is the time elapsed after activation, t_0 is the time to reach the peak tension and m and b are constants.

2.4 Constitutive subroutine

We implemented our constitutive model into the nonlinear finite element platform Abaqus using the user material subroutine VUANISOHYPER_INV. The algorithmic box 1

summarizes the input and output variables of this subroutine. The variables stateold and statenew are the inputoutput pair that allocate memory for history variables at the integration points [37]. Here, these are the stress scalars S_1^n and S_{vsc}^n from the previous equilibrium time point t_n needed to calculate the viscous stress $\bar{\mathbf{S}}_{\text{vsc}}$ at time t. We assign S_1 and $S_{\rm vsc}$ to statenew at the end of each material point calculation. In the following time step we assign these values from stateold to S_1^n and S_{vsc}^n .s Information about the deformation state is stored in the sInvariant array variable. Metrics that are available to the user are J, \bar{I}_1 , \bar{I}_{4f} , \bar{I}_{4s} and I_{8fs} . This implies that VUANISOHYPER_INV inherently assumes a volumetric-isochoric split by directly providing deformation metrics related to the isochoric deformation gradient **F**. The user implementation is supposed to return stress and tangent components through the variables,

$$\operatorname{duDi}_{i} = \frac{\partial \psi}{\partial I_{i}}$$
 and $\operatorname{d2uDiDi}_{i} = \frac{\partial^{2} \psi}{\partial I_{i}^{2}}$, (32)

where $I_i = \{J, \bar{I}_1, \bar{I}_{4f}, \bar{I}_{4s}, \bar{I}_{8fs}\}$. The algorithmic box 1 summarizes our algorithmic implementation.

Algorithm 1 Stress and tangent calculation at the integration point level.

Input : stateold, sInvariant

```
Initialize: stateold = 0
    Output: statenew, duDi, d2uDiDi
    Metrics of deformation
 1 Assign: \{J, \bar{I}_1, \bar{I}_{4f}, \bar{I}_{4s}, \bar{I}_{8fs}\} \leftarrow sInvariant
 2 Calculate: \bar{I}_{4f}^*, \bar{I}_{4s}^*, eq. (8)
    Stress and tangent components
 3 Calculate: S_J, S_1, S_{4f}, S_{4s}, S_{8fs}, eqs. (13 and 19)
 4 Calculate: S_J',\,S_1',\,S_{4\mathrm{f}}',\,S_{4\mathrm{s}}',\,S_{8\mathrm{fs}}',\,\mathrm{eqs.} (15 and 21)
    The new viscous state
 5 Assign: \{S_1^n, S_{vsc}^n\} ← stateold
 6 Calculate: S_{\rm vsc},\,S_{\rm vsc}',\,{\rm eq.}\,(27)
 7 Assign: statenew \leftarrow \{S_1, S_{\text{vsc}}\}\
    Active stress
 8 Calculate: S_{\text{act}}, S'_{\text{act}}, eq. (29)
    Return outputs
 9 Assign: duDi \leftarrow \{S_J, S_1, S_{4\mathrm{f}}, S_{4\mathrm{s}}, S_{8\mathrm{fs}}, S_{\mathrm{vsc}}, S_{\mathrm{act}}\}
10 Assign: d2uDiDi \leftarrow \{S_J', S_1', S_{4\mathrm{f}}', S_{4\mathrm{s}}', S_{8\mathrm{fs}}', S_{\mathrm{vsc}}', S_{\mathrm{act}}'\}
```

3 Computational model

In this section we describe our computational model of the beating heart. For our study, we adopt the human heart model described by Dassault Systèmes [5], using the geometry from Zygote Media [53]. This model is based on magnetic resonance imaging of a 30 year-old male heart [47].



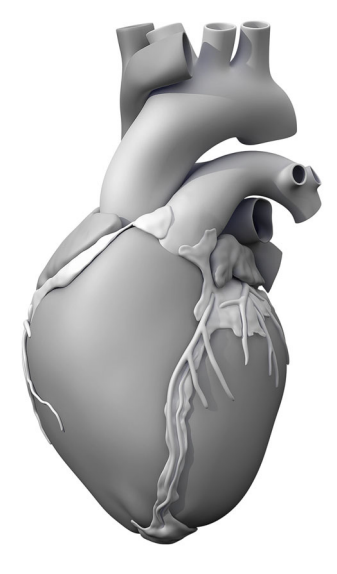


Fig. 1 Human heart model. Our three-dimensional four-chamber whole heart model was generated from high-resolution magnetic resonance images and contains the atria, ventricles, aortic arch, pulmonary artery, superior vena cava, and the coronary arteries [5]

Figure 1 shows the four-chamber CAD model of the human heart adapted from a high resolution, three-dimensional model, which includes the geometries of the ventricles and atria and the veins and arteries of the coronaries, aorta, pulmonary and superior vena cava.

3.1 Electromechanics model

An accurate simulation of mechanical contraction requires an accurate electrical activation sequence. We adopted a fast-conducting Purkinje fiber network, created using a fractal-tree generation algorithm [43], to simulate accurate conduction patterns throughout the heart. Throughout the Purkinje network and across the myocardial tissue, we employed a phenomenological electrophysiology model [3]. A fully electromechanical coupling within the finite element framework has been performed for mono-domain electrophysiology [18,20] and bi-domain electrophysiology [11, 12], and extended to electro-viscoelasticity [9]. Here the challenge is that the ultrafine spatio-temporal resolution of the electrophysiology problem makes fully-coupled simulations computationally expensive [41]. In this study, we assume a one-way electrical to mechanical coupling [5], which implies that the entire electrical and mechanical problems can be solved sequentially. This approach cannot account for mechanically-induced excitation or mechanically-modulated conduction. However, sequential solving allows for adequate discretizations of the electrical and mechanical problems and helps keep the computational cost manageable. To obtain converged electrical activation maps, we simulate five electrical heart beats. We then simulate five mechanical beats,

using the converged activation maps of the last beat of the electrical simulations.

3.2 Finite element model

We adopted the Living Heart Human Model as our finite element model [40]. In this model, the electrical and mechanical discretizations share the same geometry; however, the electrical model also incorporates a Purkinje fibers network for realistic tissue activation. We discretize the heart with 344,854 elements of which 263,028 actively contract and 81,826 only display a passive response. Figure 2 illustrates our discretization with linear T1 tetrahedral elements. Each element includes a discrete set of fiber and sheet directions \mathbf{f}_0 and \mathbf{s}_0 that characterize the orthotropic tissue behavior.

For the active response, we mapped the activation times from the electrical simulation onto the finite element mesh of the mechanical simulation and used it to trigger the mechanical contraction S_{act} . For the passive response, we adapted sets of previously calibrated parameters [23]. To match realistic pressure–volume loops, we scaled the elastic parameters $a_i = \{a, a_f, a_s, a_{fs}\}\$ and $b_i = \{b, b_f, b_s, b_{fs}\}\$ by constants A and B as summarized in Table 1. To explore the effects of viscoelasticity, we varied the viscous parameters, the relaxation time τ and the viscosity factor β [23]. We assigned a viscoelastic behavior to the ventricles and the atria shown in red in Fig. 2. Gray regions employ a hyperelastic behavior. To dampen high-frequency oscillations, we adapted a small baseline Prony-series viscoelasticity with a very short time-span. This viscous contribution is constant for each simulation and has a negligible effect on the overall results.

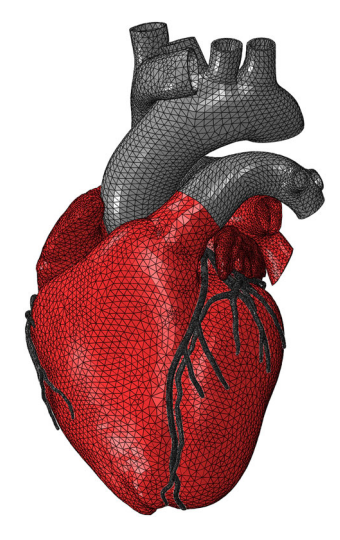


Fig. 2 Finite element model. The heart consists of 344,854 linear tetrahedral elements of which 263,028 actively contract and 81,826 only display a passive response. The heart muscle of the atria and ventricles displayed in red is viscoelastic while all other structures displayed in grey are hyperelastic



Table 1 Material parameters of the baseline-elastic passive model [23], scaled individually for each chamber to match realistic pressure-volume loops

Location	a	a_{f}	$a_{\rm s}$	a_{fs}	b	$b_{ m f}$	$b_{\rm s}$	$b_{ m fs}$
LV	0.068	2.61	0.52	11.58	0.21	14.60	0.026	2.50
RV	0.068	2.61	0.52	11.58	0.21	14.60	0.026	2.50
LA	1.680	2.63	12.79	11.65	5.24	14.70	0.630	2.52
RA	0.640	2.58	4.85	11.44	1.99	14.44	0.240	2.47

LV Left ventricle, RV Right ventricle, LA Left atrium, RA Right atrium

3.3 Circulatory model

Pressure and volume readouts from the chambers of heart provide the most important metrics to characterize the blood pumping performance. We use a fluid-cavity definition in both ventricles and atria to record pressure and volume values throughout our simulations. To obtain realistic pressure—volume loops, the mechanical model of heart needs to exchange fluid with a circulatory system model. We approximate the circulatory system using a closed-loop lumped model [5]. For the arterial, venous, and pulmonary systems we use elastic cubic volumes. In place of the valves, we use resistive elements. We account for pre-stress caused by the hemodynamic state, by mapping the reference state onto the zero-stress state [38].

3.4 Boundary conditions

We fix the heart in space using the cut planes of the aortic arch, pulmonary trunk, and superior vena cava [5]. Continuum distributed coupling constraints connect these cut planes to control nodes at the center of the cuts. Elastic springs ground the control nodes such that the motion is small during the cardiac cycle.

4 Results

To investigate the role of viscoelastic effects, in this section we compare the performance of elastic and viscoelastic material models. First, we show the sensitivity of the viscoelastic response with respect to the choice of the time window of relaxation experiments and viscous parameters τ and β . We then generate two sets of materials that include elastic and viscoelastic characteristics at different levels. We systematically compare the results from simple stress relaxation tests, pressure–volume loops, and strain distributions from simulated cardiac cycles.

4.1 Time-window sensitivity of viscoelastic model

A recent study has extensively tested the viscoelastic response of human heart tissue and observed viscous stress relaxation in an equi-biaxial stretching experiment [45]. The study applied 10% strain in the fiber and sheet directions \mathbf{f}_0 and so using a constant rate ramp function and monitored stress relaxation for 300 s. A key observation from the experimental data, the red curve in Fig. 3, is that, at the end of the recording window of 300 s, the viscous stress has not yet completely relaxed and, consequently, the stress has not reached equilibrium. A shorter or a longer time window of observation would be equivalently reasonable, because the choice of cut-off time is not unique unless the viscous stress has completely relaxed. This implies that a different time-window would result in a different set of viscous parameters τ and β . To show that this is the case, we fitted a single element viscoelastic model to the reported equi-biaxial relaxation test [45] using two different time windows. Importantly, the fitted viscous parameters only serve to illustrate the time-window sensitivity and we replaced them with more adequate parameters in our later simulations. For the elastic response, we used parameters from biaxial tests [23,45]. For the viscous response, our viscous evolution equation (22) is a first-order differential equation, which results in an exponential decay function. To approximate experimental data with this equation, we utilized the mean lifetime value associated with decaying functions.

Figure 3, top, illustrates the best fit of our single element viscoelastic model to the relaxation curve. The mean lifetime of an element, belonging to an exponentially decaying set of discrete elements is given by τ , which is the time when the population of the set is reduced to 36.79% of its initial value. To fit our viscoelastic parameters to the stress relaxation data, we match the mean lifetime of our viscous model to the timepoint where 36.79% of the viscous overstress is observed in the relaxation experiment. This fit results in a time constant of $\tau = 14.6$ s. Following the procedure for the stress relaxation test and using the observed relaxation ratio of 40%, we obtain the viscosity factor $\beta = 1.03$.

Figure 3, bottom, demonstrates the sensitivity of the viscous parameters to the recording window where we fit our model only to the first 50s of relaxation data. Using the mean lifetime value as before, we find the best fit value is $\tau=5.7\,\mathrm{s}$. At 50s we observe 32% relaxation of viscous stress. Following the experimental procedure for stretching with a relaxation ratio of 32%, we find $\beta=0.71$ to yield the best fit. We conclude that we cannot find a unique best fit, because the choice of the cut-off time of data acquisition is



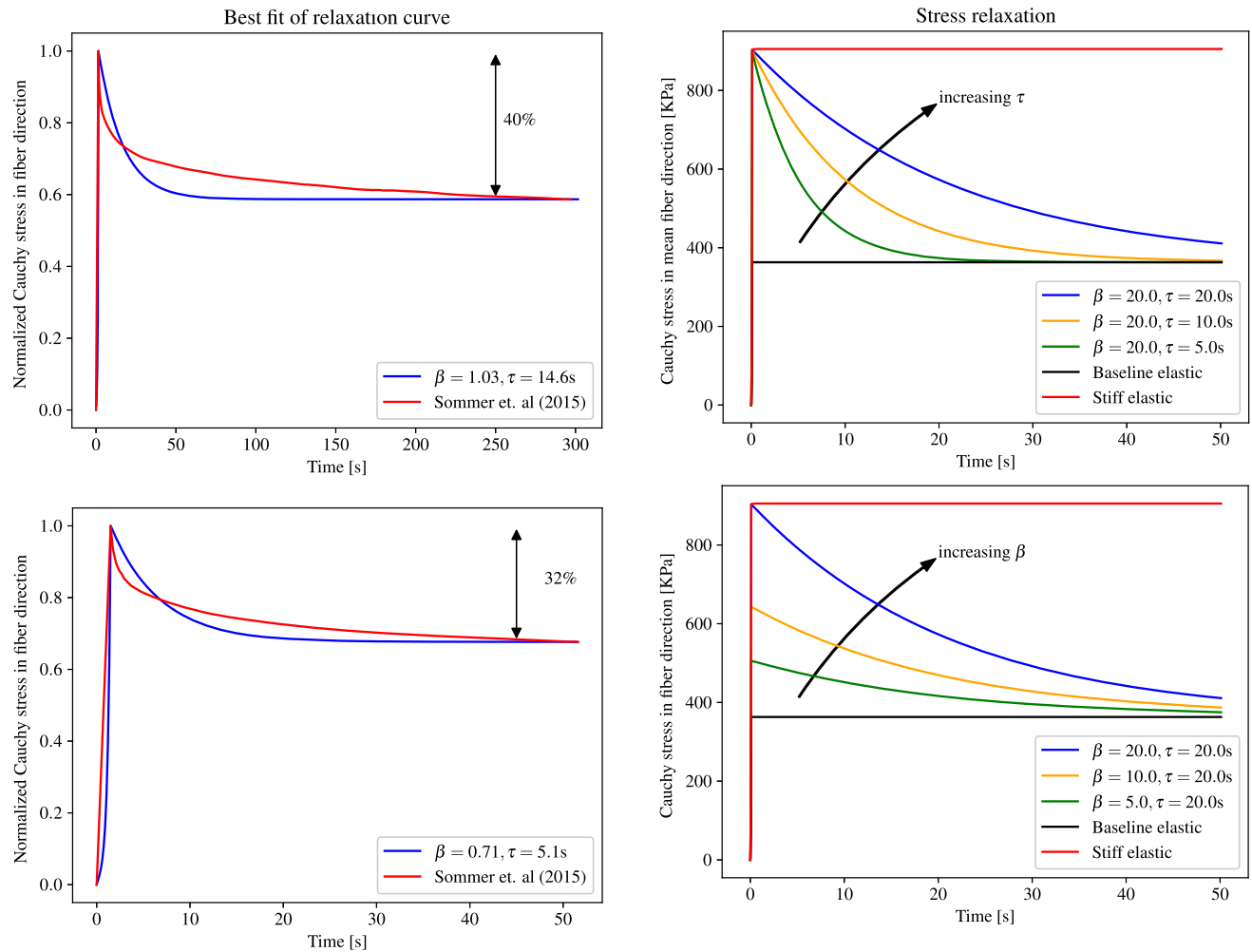


Fig. 3 Time-window sensitivity of viscoelastic model. Best fit stress relaxation curves for time window of $300\,\mathrm{s}$, $\beta=1.03$ and $\tau=14.6\,\mathrm{s}$ (top), and for time window of $50\,\mathrm{s}$, $\beta=0.71$ and $\tau=5.7\,\mathrm{s}$ (bottom). Experimental data from biaxial relaxation tests [45] with stress shown in mean fiber direction

Fig. 4 Parameter sensitivity of viscoelastic model. Stress relaxation curves for varying relaxation times τ at a fixed viscosity factor β (top), and for varying viscosity factors β at a fixed relaxation time τ (bottom). Experimental data from biaxial relaxation tests [45] with stress shown in mean fiber direction

subjective. Therefore, we study the effect of viscoelasticity using a range of parameters, instead of considering a single parameter pair obtained from a single best fit.

4.2 Parameter sensitivity of viscoelastic model

Next, we investigate the sensitivity of stress relaxation response with respect to the viscosity factor β and relaxation time τ . We compare the effects of varying the relaxation time $\tau = 5 \, \mathrm{s}$, $10 \, \mathrm{s}$, $20 \, \mathrm{s}$ for a fixed viscosity factor $\beta = 20$ and varying the viscosity factor $\beta = 5$, 10, 20 for a fixed relaxation time $\tau = 20 \, \mathrm{s}$. Two elastic materials represent extremes of the range of this viscoelastic behavior: baseline elastic, the absence of viscous over-stress, and stiff elastic, the absence of viscous relaxation. Table 1 summarizes the elastic material parameters, except for the stiff-elastic material. For the

stiff-elastic material, we scaled the a values in Table 1 by a factor 21, in order to replicate the instantaneous response of the viscous material with $\beta = 20$ and $\tau = 20$ s.

Figure 4, top, shows the stress-relaxation curves for varying relaxation times $\tau = 5 \, \mathrm{s}$, $10 \, \mathrm{s}$, $20 \, \mathrm{s}$ for a fixed viscosity factor $\beta = 20$. With increasing τ values, the initial peak stress remains the same, but stress relaxation becomes slower. For infinitely large τ , the transient response becomes constant in time and converges to that of an elastic material. With the first set of parameters, we aim to approximate the same viscous stress response to instantaneous stretching, while the transient response varies through the relaxation time constants. For comparison, we also map the stress response of the two elastic materials as the limits of the viscoelastic model: The baseline elastic material represents the behavior in the complete absence of viscosity; the stiff elastic material generates



the same instantaneous stress as viscoelastic materials, but does not display stress relaxation.

Figure 4, bottom, shows the stress–relaxation curves for varying viscosity factor $\beta = 5$, 10, 20 for a fixed relaxation time $\tau = 20$ s. With increasing β values, the initial peak stress increases, while the rate of stress relaxation for a given stress remains constant. For comparison, we also map the stress response of the two elastic materials as the limits of the viscoelastic model.

4.3 Pressure-volume loops of viscoelastic model

In this section, we compare the elastic and viscoelastic behavior of the human heart in terms of pressure–volume loops. We simulate five cardiac cycles using the viscous parameters from both parameter sets in Sect. 4.2 and extract the pressure and volume readings from the ventricular cavities. We assume that the electrical activation pattern of the heart is identical for all five cycles, such that the mechanical difference between the individual cycles is exclusively a result of the viscoelastic response of the myocardium.

Figure 5 and Table 2 summarize the pressure–volume response of the left ventricle for varying relaxation times τ at a fixed viscosity factor β during the first cardiac cycles, top, and fifth cardiac cycles, bottom.

The first thing to note in the Fig. 5 is the difference between the two elastic cases that are representative of viscous extremes, baseline elastic shown in black and stiff elastic shown in red. The maximum pressure and volume are lower for the stiff elastic material compared to baseline elastic. In Table 2, we see the stiff elastic material results in a 10% drop in ejection fraction as a result of the 36mL drop in end-diastolic volume compared to baseline elastic.

Our second observation from the Fig. 5 is that all viscous materials resulted in pressure–volume loops that are very close to each other. The four-fold difference in the relaxation time τ caused insignificant differences in the performance metrics of pressure, volume, and ejection fraction.

During the first cardiac cycle, all viscous simulations with fixed viscosity factor β closely resemble the red curve of the stiff elastic material. This is a result of the relatively short time of a single cardiac cycle, approximately 1 s or 1.3 s including the pre-inflation, compared to the characteristic relaxation times τ that vary from 5 to 20 s. We conclude that, within the analyzed viscous parameter range for β and τ , we do not observe significant effects of viscous relaxation. This implies that the pressure–volume loops of a viscoelastic material can be equally well approximated by a stiffer hyperelastic material model.

During the fifth cardiac cycle, we see a slightly different picture. Both elastic models display slightly different pressure–volume loops between the first and fifth cycles. This is because that the simulation starts from a zero stress

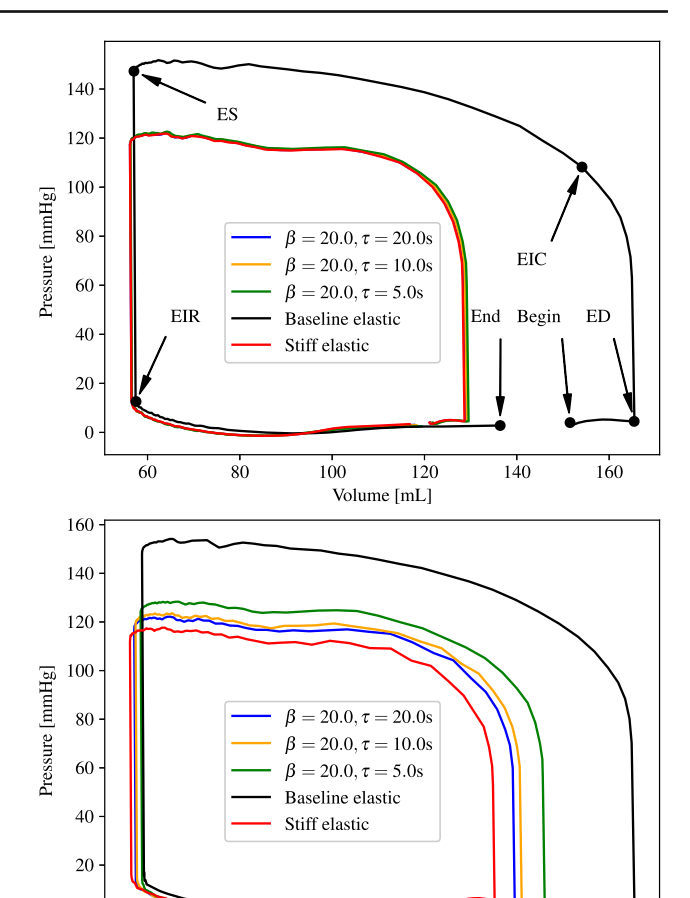


Fig. 5 Pressure–volume loop sensitivity of viscoelastic model. Pressure volume loops for varying relaxation times τ at a fixed viscosity factor β , for first cardiac cycle (top) and fifth cardiac cycle (bottom). *ED* End diastole, *EIC* End-isovolumic contraction, *ES* End systole, *EIR* End-isovolumic relaxation

100

Volume [mL]

120

140

160

state instead of starting from a converged cyclic simulation. Between the first cycle and the fifth cycle, the difference of ejection fraction between both elastic extremes dropped from 10% to 6%. In addition, the pressure–volume responses of the viscous models have moved away from the stiff elastic model. This is a result of the larger timespan of five cardiac cycles, approximately 5 s, that reveal the viscous relaxation effects on the pressure–volume loops. The most notable difference of the fifth cardiac cycle is that the blue curve with the largest relaxation time of $\tau = 20 \, \mathrm{s}$ stays closest to the red curve of the stiff elastic model, because its relaxation takes longest. The green curve with the smallest relaxation time of $\tau = 5 \, \mathrm{s}$ has separated most from the stiff elastic model the, because of its short characteristic relaxation time.

Figure 6 and Table 3 summarize the pressure–volume response of the left ventricle for varying viscosity factors β at a fixed relaxation time τ during the first cardiac cycles, top, and fifth cardiac cycles, bottom.



 Table 2
 Pressure-volume loop

 sensitivity of viscoelastic model

Left ventricle 1st cycle	Max pressure (mmHg)	Max volume (mL)	Ejection fraction (%)	
$\beta = 20, \tau = 20 \mathrm{s}$	122	129	56	
$\beta = 20, \tau = 10 \mathrm{s}$	123	129	56	
$\beta = 20, \tau = 5 \mathrm{s}$	123	129	56	
Baseline elastic	152	165	66	
Stiff elastic	122	129	56	
Left ventricle 5th cycle	Max pressure (mmHg)	Max volume (mL)	Ejection fraction (%)	
Left ventricle 5th cycle $\beta = 20, \tau = 20 \text{ s}$	Max pressure (mmHg) 122	Max volume (mL)	Ejection fraction (%) 60	
	1 (2)			
$\beta = 20, \tau = 20 \mathrm{s}$	122	133	60	
$\beta = 20, \tau = 20 \text{ s}$ $\beta = 20, \tau = 10 \text{ s}$	122	133 134	60 61	

Maximum pressure, maximum volume, and ejection fraction from pressure–volume loops for varying relaxation times τ at a fixed viscosity factor β , for first cardiac cycle (top) and fifth cardiac cycle (bottom)

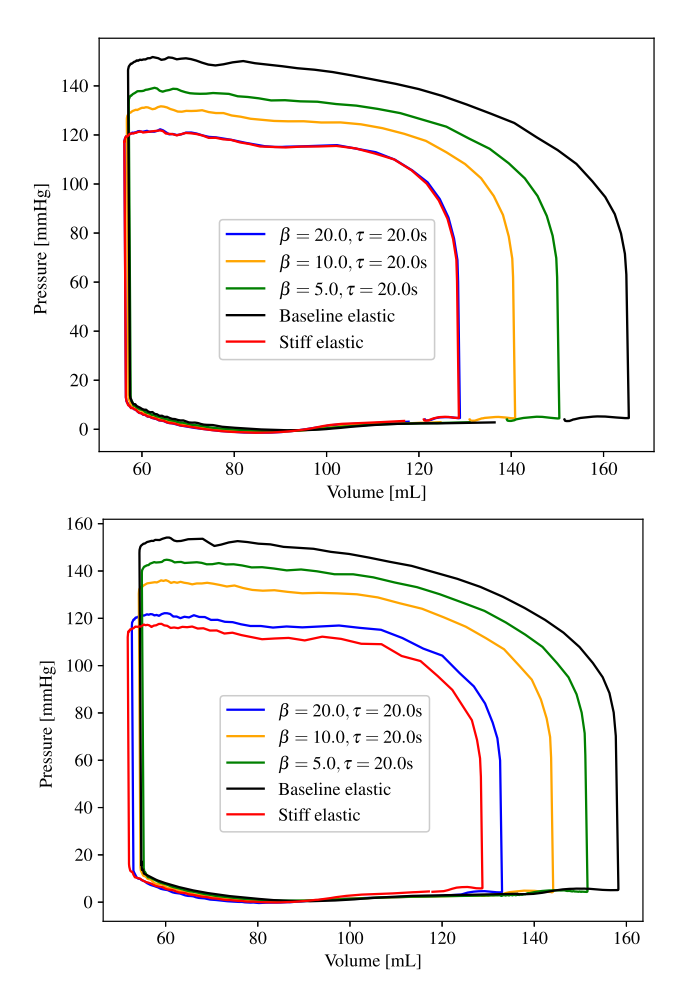


Fig. 6 Pressure–volume loop sensitivity of viscoelastic model. Pressure volume loops for varying viscosity factors β at a fixed relaxation time τ , for first cardiac cycle (top) and fifth cardiac cycle (bottom). *ED* End diastole, *EIC* End-isovolumic contraction, *ES* End systole, *EIR* End-isovolumic relaxation

The first thing to note is that the blue curves of the viscoelastic model with $\beta=20$ and $\tau=20\,\mathrm{s}$, and the red and black curves of the stiff elastic and baseline elastic models are shared with the previous simulations in Fig. 5 and Table 2. A notable difference between the previous simulation with varying τ values in Fig. 5 is that the mechanical response, and with it the pressure–volume loops, are altered significantly by varying the β parameter. During the first cardiac cycle, we already observe a clear separation of all three viscoelastic models. During the fifth cardiac cycle, the pressure–volume loops of all viscous models have moved away from the stiff elastic material and towards the baseline elastic material. This confirms the trend that we have observed in the stress relaxation curves of our initial sensitivity analysis in Fig. 4.

4.4 Fiber strain across the heart

Lastly, we investigate the distribution of strains in fiber direction across the heart throughout the first and fifth cardiac cycle. Figure 7 shows the spatio-temporal distribution of the Green Lagrange fiber strains throughout the first cardiac cycle for the stiff elastic model, and two viscoelastic models with $\beta = 20$ and $\tau = 20$ s and with $\beta = 20$ and $\tau = 5$ s. Recall that the pressure–volume loops of the left ventricle in Fig. 5, top, suggest that the pump function of these three material models is similar. The strain fields in Fig. 9 support this observation. The three rows of the elastic and two viscoelastic models show virtually the same contour plots. Figure 9, top, provides a quantitative comparison of the fiber strains throughout the first cycle. Here, we plot the strains only for the left ventricle, where the horizontal lines mark the mean values in the strain distribution. As evident from the plot, the strain distributions are almost identical which supports the argument that viscous relaxation does not play an important role in single-beat simulations.



Table 3 Pressure–volume loop sensitivity of viscoelastic model

eft ventricle 1st cycle Max pressure (mmHg		Max volume (mL)	Ejection fraction (%)	
$\beta = 20, \tau = 20 \mathrm{s}$	122	129	56	
$\beta = 10, \tau = 20 \mathrm{s}$	132	141	60	
$\beta = 5$, $\tau = 20$ s	139	150	62	
Baseline elastic	152	165	66	
Stiff elastic	122	129	56	
Left ventricle 5th cycle	Max pressure (mmHg)	Max volume (mL)	Ejection fraction	
$\beta = 20, \tau = 20 \mathrm{s}$	122	133	60	
$\beta = 10, \tau = 20 \mathrm{s}$	136	144	62	
$\beta = 5$, $\tau = 20$ s	145	152	64	
Baseline elastic	154	158	66	
Stiff elastic	118	129	60	

Maximum pressure, maximum volume, and ejection fraction from pressure–volume loops for varying viscosity factors β at a fixed relaxation time τ for first cardiac cycle (top) and fifth cardiac cycle (bottom)

Fig. 7 Fiber strain distribution across the heart. Spatio-temporal evolution of Green–Lagrange strains in fiber direction E_{11} throughout the first cardiac cycle with stiff elastic model (top), β = 20 and τ = 20 s (middle), and β = 20 and τ = 5 s (bottom). Time points are indicated in Fig. 5 (top). ED End diastole, EIC End-isovolumic contraction, ES End systole, EIR End-isovolumic relaxation

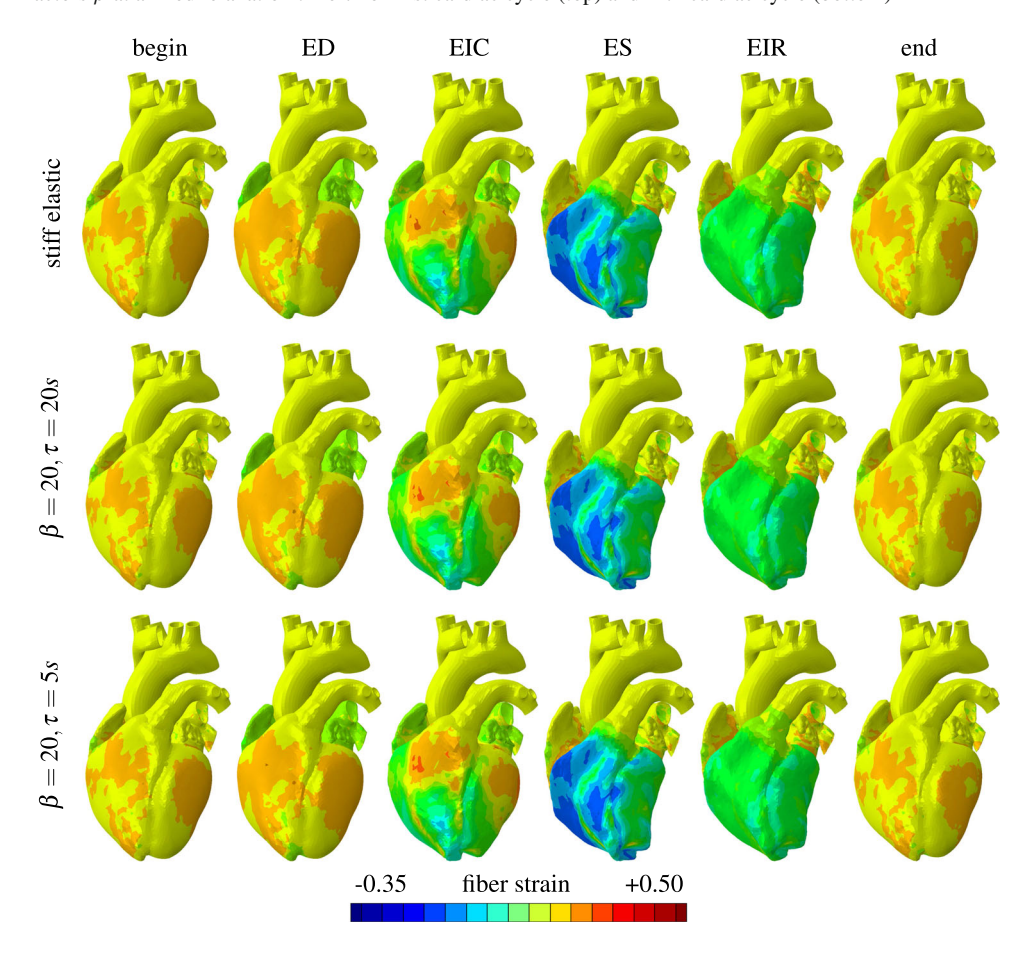
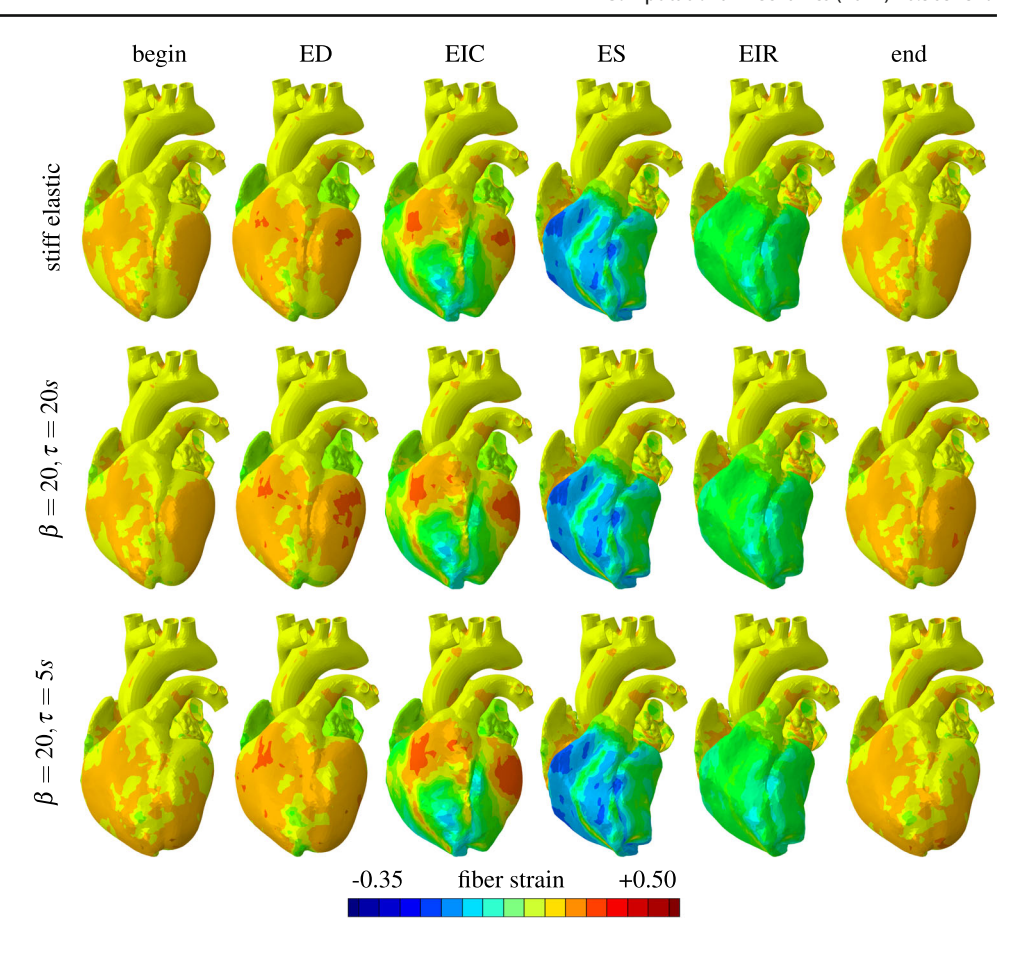


Figure 8 shows the spatio-temporal distribution of the Green Lagrange fiber strains, but now throughout the fifth cardiac cycle. We can observe clear differences in the strain contours between the stiff elastic model and the two viscoelastic models with $\beta=20$ and $\tau=20$ s and with $\beta=20$ and $\tau=5$ s. Although not obvious, these strain differences are most apparent at end diastole and end-isovolumic contraction

in the second and third columns. For these time points, the high strain regions shown in red differ, e.g., in the upper-left ventricular wall. When comparing the end-diastolic state in the second column, we observe that the high-strain regions of left ventricle are largest for the $\beta=20$ and $\tau=20$ s model, followed by the stiff elastic model, and the $\beta=20$ and $\tau=5$ s model. Figure 9, bottom, reveals a similar result, with largest



Fig. 8 Fiber strain distribution across the heart. Spatio-temporal evolution of Green–Lagrange strains in fiber direction E_{11} throughout the fifth cardiac cycle with stiff elastic model (top), $\beta = 20$ and $\tau = 20$ s (middle), and $\beta = 20$ and $\tau = 5$ s (bottom). Time points are indicated in Fig. 5 (top). *ED* End diastole, *EIC* End-isovolumic contraction, *ES* End systole, *EIR* End-isovolumic relaxation



averaged fiber strains for $\beta=20$ and $\tau=20\,\mathrm{s}$, followed by the stiff elastic model and $\beta=20$ and $\tau=5\,\mathrm{s}$. These results add another perspective to the pressure–volume loops in Fig. 5, bottom, where the stiff elastic model had the smallest end-diastolic volume followed by the $\beta=20$ and $\tau=20\,\mathrm{s}$ and the $\beta=20$ and $\tau=5\,\mathrm{s}$ models. These observations suggest that the strain state of a whole heart model with viscoelastic behavior is too complex to infer from low fidelity data such as pressure–volume loops. We also observe that the violin plots in Fig. 9 reveal differing strains for different material models throughout the fifth cardiac cycle, in contrast to the similar strain distributions throughout the first cycle. This difference points to the importance of large-enough simulation windows simulations, to capture the full viscoelastic response.

5 Discussion

The objective of this study was to investigate the effect of viscoelasticity in cardiac modeling. Towards this goal, we used a finite-deformation viscoelastic continuum model. To integrate the orthotropic character of cardiac muscle tissue, we accounted for two families of elastic fibers, and

attributed the viscoelasticity exclusively to the matrix component. Specifically, we adopted a viscoelastic version of the Holzapfel-Ogden model and assumed an exponential decay of the transient viscous stress. We implemented our viscoelastic constitutive model into the Living Heart Project, which, to date, had only utilized a baseline elastic model.

Our study underlines the inherent subjectivity of fitting viscoelastic material parameters to experimental data and, more importantly, the relevance of the window of observation. We performed a sensitivity study to highlight the effects of the simplest possible viscoelastic model and explored the sensitivity of stress—relaxation curves, pressure—volume loops, and strain profiles with respect to different viscoelastic parameterizations. We studied two sets of viscous parameters and compared both against two elastic parameterizations.

Our comparisons of pressure–volume loops and strain profiles revealed that tissue viscosity generally has a notable effect on the resulting pressure–volume loops: Heart muscle undergoes high peak strain rates during contraction and the viscous contributions to the muscle stiffness result in visibly shifted pressure–volume loops. However, the viscoelastic nature of the tissue has negligible effects on the strain profile throughout a given cardiac cycle. While viscous relaxation is relevant within time windows on the order of tens of seconds,



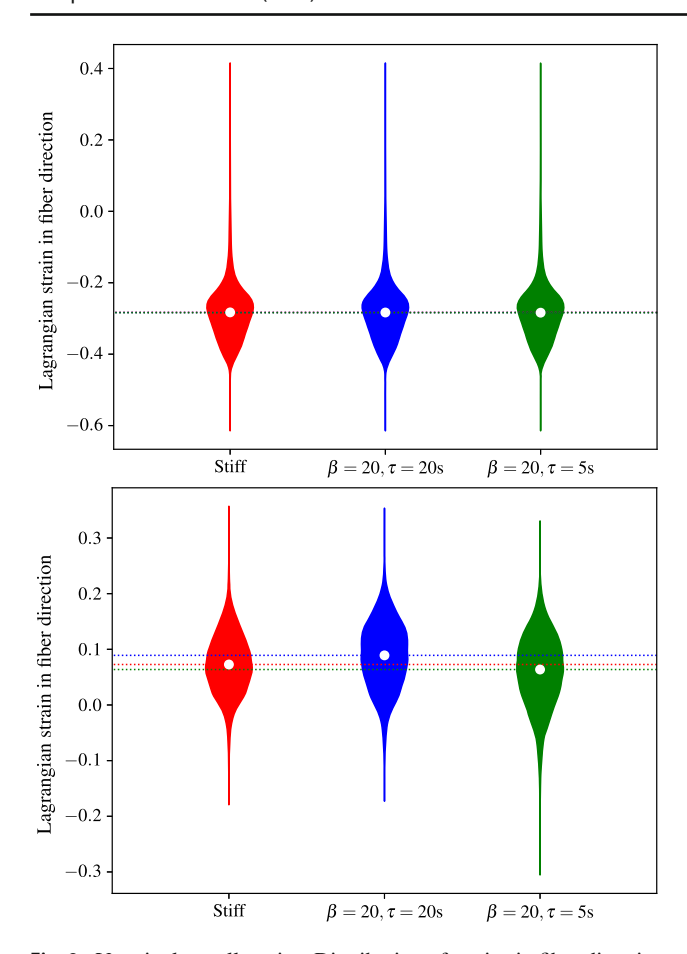


Fig. 9 Ventricular wall strains. Distribution of strains in fiber direction in the left ventricular wall for varying relaxation times τ at a fixed viscosity factor β for first cardiac cycle (top) and fifth cardiac cycle (bottom). Strains are recorded at end diastole

this phenomenon seems to be less important within physiological contraction times on the order of a tenth of a second. However, multiple successive cardiac cycles will span a time window that is long enough to reveal the effects of viscous relaxation. In such multi-beat simulations, we observed that the pressure–volume loops shift with each cycle. In essence, relaxation is significant between cardiac cycles, even though it is not significant within an individual cycles. This suggests that for single-beat simulations of cardiac mechanics, we can reasonably well approximate the constitutive behavior of the heart muscle tissue as hyperelastic. However, for simulations involving more than one beat, myocardium viscosity can significantly alter the results. This implies that, if viscoelastic models are used, they should be run for multiple cycles until they reach a fully converged steady state.

Our study has a few limitations, rooted in our motivation of using a simple model to probe viscoelastic effects, and on the limited availability of experimental data: First, we employed a simple viscoelastic model based on a single rheological element with only two viscous parameters. While a higher-order model would have provided a better fit to the experimental data, the inherent sensitivity with respect to the fitted time window would remain. Second, we have only studied a certain range of viscoelastic parameters that are in agreement with the range of suggested parameters in the literature. Our conclusions may change outside this parameter range, and also when the heart rate deviates much from its healthy range of about 1/s. Third, we have only considered viscosity for the isotropic matrix component. Studies have shown that the extracellular matrix is the major contributor of tissue viscosity [36]. Unlike fiber viscosity that only acts in tension, matrix viscosity can be activated in both stretch and shear deformation modes. Fourth, a limitation of our continuum model is the use of the volumetric-isochoric decomposition of the deformation gradient in conjunction with compressible material parameters. We closely monitor our deformations to ensure that they are not dominated by the volumetric expansion, which remains within $\pm 1.7\%$ throughout the five cardiac cycles. Last, an important limitation of our study is that our viscous parameter selection is based on ex vivo tissue experiments on isolated cubes of myocardial tissue which are not representative of in-vivo conditions.

In view of these limitations, we believe that the experimental characterization of the viscoelastic response of cardiac tissue will be an important next step to identify the range of validity of current hyperelastic models. Under physiological conditions, cardiac tissue experiences relatively high strain rates, and it is important to probe the tissue under conditions that mimic this physiological regime. We believe that the value of future viscoelasticity experiments will lie in focusing on the viscoelastic response within the time-scales of a cardiac cycle or even smaller. Understanding the role of tissue viscosity is important whenmodeling healthy hearts as well as pathological conditions and we believe that it has the potential of making a dramatic impact on the accuracy of simulation results.

Acknowledgements We acknowledge support through the NSF Grant SI2-SSI 1663671 'The SimCardio open source multi-physics cardiac modeling package' and the NIH Grant R01 HL131823 'A new framework for understanding the mechanisms of diastolic dysfunction'.

References

- AHA Statistical Update (2020) Heart disease and stroke statistics— 2020 update: a report from the American Heart Association. Circulation 141:e139–e596
- Alber M, Buganza Tepole A, Cannon W, De S, Dura-Bernal S, Garikipati K, Karniadakis G, Lytton WW, Perdikaris P, Petzold L, Kuhl E (2019) Integrating machine learning and multiscale modeling: perspectives, challenges, and opportunities in the biological, biomedical, and behavioral sciences. npj Digit Med 2:115



- Aliev RR, Panfilov AV (1996) A simple two-variable model of cardiac excitation. Chaos Solitons Fractals 7(3):293–301
- Ambrosi D, Pezzuto S (2012) Active stress vs. active strain in mechanobiology: constitutive issues. J Elast 107:199–212
- Baillargeon B, Rebelo N, Fox DD, Taylor RL, Kuhl E (2014) The living heart project: a robust and integrative simulator for human heart function. Eur J Mech A/Solids 48:38–47
- Berberoğlu E, Solmaz HO, Göktepe S (2014) Computational modeling of coupled cardiac electromechanics incorporating cardiac dysfunctions. Eur J Mech A/Solids 48:60–73
- Cansiz B, Dal H, Kaliske M (2015) An orthotropic viscoelastic material model for passive myocardium: theory and algorithmic treatment. Comput Methods Biomech Biomed Eng 18:1160–1172
- Cansiz B, Dal H, Kaliske M (2017) Computational cardiology: a modified Hill model to describe the electro-visco-elasticity of the myocardium. Comput Methods Appl Mech Eng 315:434

 –466
- Cansiz B, Sveric K, Ibrahim K, Strasser RH, Linke A, Kaliske M (2018) Towards predictive computer simulations in cardiology: finite element analysis of personalized heart models. ZAMM-J Appl Math Mech 98–12:2155–2176
- Chabiniok R, Wang V, Hadjicharalambous M, Asner L, Lee J, Sermesant M, Kuhl E, Young A, Moireau P, Nash M, Chapelle D, Nordsletten DA (2016) Multiphysics and multiscale modeling, data-model fusion and integration of organ physiology in the clinic: ventricular cardiac mechanics. Interface Focus 6:20150083
- Dal H, Göktepe S, Kaliske M, Kuhl E (2012) A fully implicit finite element method for bidomain models of cardiac electrophysiology. Comput Methods Biomech Biomed Eng 15–6:645–656
- Dal H, Göktepe S, Kaliske M, Kuhl E (2013) A fully implicit finite element method for bidomain models of cardiac electromechanics. Comput Methods Appl Mech Eng 253:323–336
- Dal H (2019) A quasi-incompressible and quasi-inextensible element formulation for transversely isotropic materials. Int J Numer Methods Eng 117:118–140
- Dokos S, Smaill BH, Young AA, LeGrice IJ (2002) Shear properties of passive ventricular myocardium. Am J Physiol Heart Circ Physiol 283:H2650–H2659
- Eriksson TS, Prassl AJ, Plank G, Holzapfel GA (2013) Modeling the dispersion in electromechanically coupled myocardium. Int J Numer Methods Biomed Eng 29:1267–1284
- Genet M, Lee LC, Baillargeon B, Guccione JM, Kuhl E (2016) Modeling pathologies of systolic and diastolic heart failure. Ann Biomed Eng 44:112–127
- Göktepe S, Kuhl E (2009) Computational modeling of electrophysiology: a novel finite element approach. Int J Numer Methods Eng 79:156–178
- Göktepe S, Kuhl E (2010) Electromechanics of the heart—a unified approach to the strongly coupled excitation—contraction problem. Comput Mech 45:227–243
- Göktepe S, Acharya SNS, Kuhl E (2011) Computational modeling of passive myocardium. Int J Numer Methods Biomed Eng 27:1–12
- Göktepe S, Menzel A, Kuhl E (2014) The generalized Hill model: a kinematic approach towards active muscle contraction. J Mech Phys Solids 72:20–39
- Granzier HL, Siegfried L (2004) The giant protein titin: a major player in myocardial mechanics, signaling, and disease. Circ Res 94:284–295
- Guccione JM, Moonly SM, Moustakidis P, Costa KD, Moulton MJ, Ratcliffe MB, Pasque MK (2001) Mechanism underlying mechanical dysfunction in the border zone of left ventricular aneurysm: a finite element model study. Ann Thorac Surg 71:654–662
- Gültekin O, Sommer G, Holzapfel GA (2016) An orthotropic viscoelastic model for the passive myocardium: continuum basis and numerical treatment. Comput Methods Biomech Biomed Eng 19:1647–1664

- Gültekin O, Dal H, Holzapfel GA (2019) On the quasiincompressible finite element analysis of anisotropic hyperelastic materials. Comput Mech 63:443–453
- Helfenstein J, Jabareen M, Mazza E, Govindjee S (2010) On non-physical response in models for fiber-reinforced hyperelastic materials. Int J Solids Struct 47:2056–2061
- Hill AV (1938) The heat of shortening and the dynamic constants of muscle. Proc R Soc Lond Ser B Biol Sci 126:136–195
- Holzapfel GA, Simo JC (1996) A new viscoelastic constitutive model for continuous media at finite thermomechanical changes. Int J Solids Struct 33:3019–3034
- Holzapfel GA (2002) Nonlinear solid mechanics: a continuum approach for engineering science. Meccanica 37(4):489–490
- Holzapfel GA, Ogden RW (2009) Constitutive modelling of passive myocardium: a structurally based framework for material characterization. Philos Trans R Soc Lond 367:3445–3475
- Humphrey JD, Strumpf RK, Yin FCP (1990) Determination of a constitutive relation for passive myocardium: I. A new functional form
- Kaliske M (2000) A formulation of elasticity and viscoelasticity for fibre reinforced material at small and finite strains. Comput Methods Appl Mech Eng 185:225–243
- Liu J, Marsden AL (2018) A unified continuum and variational multiscale formulation for fluids, solids, and fluid-structure interaction. Comput Methods Appl Mech Eng 337:549–597
- McEvoy E, Holzapfel GA, McGarry P (2018) Compressibility and anisotropy of the ventricular myocardium: experimental analysis and microstructural modeling. J Biomech Eng 140:081004
- Nash MP, Panfilov AV (2004) Electromechanical model of excitable tissue to study reentrant cardiac arrhythmias. Prog Biophys Mol Biol 85:501–522
- Nedjar B (2007) An anisotropic viscoelastic fibre-matrix model at finite strains: continuum formulation and computational aspects. Comput Methods Appl Mech Eng 196:1745–1756
- Nordsletten D, Capilnasiu A, Zhang W, Wittgenstein A, Hadjicharalambous M, Sommer G, Sinkus R, Holzapfel GA (2021) A viscoelastic model for human myocardium. arXiv preprint arXiv:2105.06671
- Ostwald R, Kuhl E, Menzel A (2019) On the implementation of finite deformation gradient-enhanced damage models. Comput Mech 64:847–877
- 38. Peirlinck M, De Beule M, Segers P, Rebelo N (2018) A modular inverse elastostatics approach to resolve the pressure-induced stress state for in vivo imaging based cardiovascular modeling. J Mech Behav Biomed Mater 85:124–133
- Peirlinck M, Costabal FS, Sack KL, Choy JS, Kassab GS, Guccione JM, De Beule M, Segers P, Kuhl E (2019) Using machine learning to characterize heart failure across the scales. Biomech Model Mechanobiol 18:1987–2001
- Peirlinck M, Costabal FS, Yao J, Guccione JM, Tripathy S, Wang Y, Ozturk D, Segars P, Morrison TM, Levine S, Kuhl E (2021) Precision medicine in human heart modeling. Biomech Model Mechanobiol 20:803–831
- Peirlinck M, Yao J, Sahli Costabal F, Kuhl E (2022) How drugs modulate the performance of the human heart. Comput Mech. https://doi.org/10.1007/s00466-022-02146-1
- Rubiano A, Qi Y, Guzzo D, Rathinasabapathy A, Rowe K, Pepine C, Simmons C (2016) Stem cell therapy restores viscoelastic properties of myocardium in rat model of hypertension. J Mech Behav Biomed Mater 59:71–77
- Sahli Costabal F, Hurtado DE, Kuhl E (2016) Generating Purkinje networks in the human heart. J Biomech 49(12):2455–2465
- Sahli Costabal F, Concha FA, Hurtado DE, Kuhl E (2017) The importance of mechano-electrical feedback and inertia in cardiac electromechanics. Comput Methods Appl Mech Eng 320:352–368



- Sommer G, Schriefl AJ, Andrä M, Sacherer M, Viertler C, Wolinski H, Holzapfel GA (2015) Biomechanical properties and microstructure of human ventricular myocardium. Acta Biomaterialia 24:172–192
- 46. Sommer G, Haspinger DC, Andrä M, Sacherer M, Viertler C, Regitnig P, Holzapfel GA (2015) Quantification of shear deformations and corresponding stresses in the biaxially tested human myocardium. Ann Biomed Eng 43:2334–2348
- 47. St Pierre SR, Peirlinck M, Kuhl E (2022) Sex matters: a comprehensive comparison of female and male hearts. Front Physiol 13:831179
- Stroud JD, Baicu CF, Barnes MA, Spinale FG, Zile MR (2002) Viscoelastic properties of pressure overload hypertrophied myocardium: effect of serine protease treatment. Am J Physiol Heart Circ Physiol 282:H2324–H2335
- Updegrove A, Wilson NM, Merkow J, Lan H, Marsden AL, Shadden SC (2017) SimVascular: an open source pipeline for cardiovascular simulation. Ann Biomed Eng 45(3):525–541

- Walker JC, Ratcliffe MB, Zhang P, Wallace AW, Fata B, Hsu EW, Saloner D, Guccione JM (2005) MRI-based finite-element analysis of left ventricular aneurysm. Am J Physiol Heart Circ Physiol 289:H692–H700
- Yang M, Taber LA (1991) The possible role of poroelasticity in the apparent viscoelastic behavior of passive cardiac muscle. J Biomech 24:587–597
- Yao J, Varner VD, Brilli LL, Young JM, Taber LA, Perucchio R (2012) Viscoelastic material properties of the myocardium and cardiac jelly in the looping chick heart. J Biomech Eng 134:024502
- Zygote Media Group Inc. (2014) Zygote solid 3D heart generations
 I & II development report. Technical development of 3D anatomical systems

Publisher's Note Springer Nature remains neutral with regard to jurisdictional claims in published maps and institutional affiliations.

